Nano Research
DOI
Research Article

ISSN 1998-0124
CN 11-5974/O4

Hierarchical Sb-Ni nanoarrays as robust binder-free anodes for high-performance sodium-ion half cells and full Cells

Liying Liang, Yang Xu, Liaoyong Wen, Yueliang Li, Min Zhou, Chengliang Wang, Huaping Zhao, Ute Kaiser, and Yong Lei (✉)

[1] *Institute of Physics & IMN MacroNano (ZIK), Ilmenau University of Technology, Professor Schmidt Strasse 26, 98693 Ilmenau, Germany*
[2] *Central Facility for Electron Microscopy, Electron Microscopy Group of Materials Science, Ulm University, Albert-Einstein-Allee 11, 89081 Ulm, Germany*

Received: day month year
Revised: day month year
Accepted: day month year

KEYWORDS
hierarchical Sb-Ni nanoarrays, binder-free anode, capacitive charge storage, Na-ion full cell

ABSTRACT

A novel hierarchical electrode composed of Sb nanoplates on Ni nanorod arrays is proposed to tackle the issues of the rapidly fading capacity and poor rate capability of Sb materials for Na-ion batteries. The 3D Sb-Ni nanoarray anode demonstrates the synergistic effect of the 2D nanoplates, open conductive array structure, and strong structural integrity, for which a capacitive behavior is verified by kinetics analysis, rendering excellent Na-storage performance by tailoring electrode nanostructures. When used as binder-free SIB anode, it exhibits high capacity retention of 80% over 200 cycles at a high current density of 0.5 A g^{-1}, and excellent rate capacity up to 20 A g^{-1} with the capacity of 580 mAh g^{-1}. Moreover, a P2-$Na_{2/3}Ni_{1/3}Mn_{2/3}O_2$//3D Sb-Ni nanoarrays full cell delivers a highly reversible capacity of 579.8 mAh g^{-1} over 200 cycles and a high energy density of 100 Wh kg^{-1}. This design strategy may work in other electrode materials for fast and stable Na-storage.

1 Introduction

With the consumption of fossil fuel as well as increasing environmental pollution, the development of more advanced energy storage and conversion devices is urgently needed [1]. As the most promising alternative to lithium-ion batteries (LIBs), rechargeable sodium-ion batteries (SIBs) have received growing attention for large-scale energy storage applications, due to the natural abundance of sodium [2,3]. However, one of the challenges to commercialize Na-ion batteries is to exploit suitable anode materials to host Na ions which has a larger radius than that of Li ions [4,5]. Commercial graphite, widely used as LIB anode, fails to react with sodium effectively, due to poor intercalation property for the larger Na^+ radius [6]. Up to now, among various anode material candidates, metallic Sb is quite attractive because of its high theoretical capacity (660 mAh g^{-1}) and a relatively safe operating potential of

Address correspondence to yong.lei@tu-ilmenau.de

around 0.4 V (Na^+/Na) [7,8]. In spite of these advantages, the main bottleneck for the implementation of Sb anode is its large volume change (~390%) during cycling [9,10], because it is easy to induce pulverization of Sb materials and thus electrical isolation from the current collector, consequently showing rapid capacity degradation and poor rate capability [5,11].

To address the issue of huge volume change, one effective method is to design integrated electrodes in which nanosized active materials are grafted to a secondary matrix [12-16]. The unique electrodes can not only provide good accommodation of large volume variation, but also show high ion accessibility and fast electron transport, the combination of which are three indispensable elements for high electrochemical performance. Since the electrochemical properties of materials have intimate connections with the design at the nanoscale, increasing attention has been paid to designing metallic Sb with special morphologies, especially in terms of particle size and interparticle space [17-19]. Previous reports have shown that decreasing the dimension of Sb into nanometer range could enhance the tolerance of stress change during alloying/dealloying, and shorten electronic and ionic transport pathways, hence gaining a high capacity, long cycling life, and good rate capability [20-22]. For instance, monodisperse antimony nanocrystals were used as SIB anodes and delivered a high capacity of about 550 and 520 mAh g^{-1} at current densities of 5.28 and 13.2 A g^{-1}, respectively [18]. A nanoporous-antimony anode was fabricated to show a high capacity of 573.8 mAh g^{-1} after 200 cycles at a rate of 100 mA g^{-1} [23]. Recently, nanoplates have attracted significant attention as a result of their unique structural and mechanical strength with high surface-to-volume ratios. Nanoplates-based electrode materials exhibit short ion diffusion length, and large surface contact with electrolyte and conductive materials which is beneficial to improve capacitive charge storage, thus rendering excellent rate performance and high power density.

Three dimensional (3D) nanoarrayed current collectors as the secondary matrix for the graft of active materials have been proven as a promising electrode configuration. This 3D conductive open network creates open channels and increases contact area between current collectors and active materials, resulting in fast ion/electron transport and large electrode/electrolyte interface area. The unique 3D core/shell structures could effectively inhibit the aggregation of active materials and thus show better accommodation of large volume change upon cycling [24-28]. Conventional electrodes adopt a flat structure and include inactive additives such as polymeric binders, which often suffer from insufficient ion permeation and block electron transport caused by insulated binder [29, 30]. By contrast, 3D additive-free nanoarrayed electrodes with excellent electric conductivity and self-integrity can efficiently resolve these issues and omit the complex electrode fabrication processes [31, 32]. Overall, the above features lead to enhanced cycle life and high rate capability [24-33].

Herein, we rationally designed a new 3D nanostructured configuration for Sb anode material, namely hierarchical electrode composed of Sb nanoplates on Ni nanorod arrays (3D Sb-Ni nanoarrays) for high-performance SIBs. This heterostructured electrode combines the advantages of 2D nanoplates, open conductive array structure, and strong structural integrity. These joint electrode designs significantly promote the electron and ion transport and the accommodation of large volume change. As binder-free SIB anodes, 3D Sb-Ni nanoarrays showed high capacity, long cycling life, and excellent rate capability for not only Na-ion half cells but also full cells. The encouraging results may shed lights on SIBs anodes and provoke deeper understanding of material engineering strategies to improve SIBs performance.

2 Results and Discussion

2.1 Structural characterization

The strategy for preparing 3D Sb-Ni nanoarrays is schematically depicted in Figure 1. Firstly, a through-pore anodized aluminum oxide (AAO) template with conductive substrate (Figure 1a) is prepared according to our previous reports [34]. The scanning electron microscopy (SEM) image in Figure 1d clearly reveals uniform AAO template with the pore size of about 210 nm. Next, 3D Ni nanorod

arrays are fabricated by electrodeposition through AAO template that was subsequently dissolved (Figure 1b). Figure 1e displays that Ni nanorods are smooth and vertically aligned to the substrate, with about 210 nm diameters and 190 nm interval distance among nanorods. The unique Ni nanorod arrays could be used as efficient current collectors and skeletons for directly spontaneous deposition of active materials with a high specific surface area and active sites. The fabrication is finally finished by growing Sb nanoplates on Ni nanorod arrays using electrodeposition with the assistance of vacuum. As a result, 3D Sb-Ni nanoarrays with robust adhesion are achieved as binder-free SIB anodes, as shown in Figure 1c. Such an electrode configuration can enable fast ion/electron transport, large electrode/electrolyte interface area, and accommodate the volume change upon cycling, thus ensuring the stability of electrode structure. Figure 1f reveals the high-quality and uniform 3D Sb-Ni nanoarrays in a large scale, from which rough surface of arrays can be seen, indicating the successful deposition of Sb. Moreover, there is much uniform interspace available among arrays, suggesting a highway of electrolyte penetration and a good volume variation accommodation. The magnified SEM image (Figure 1g) clearly presents the formation of Sb nanoplates grown on Ni nanorod arrays, in which the Sb shell is composed of randomly oriented nanoplates that form a hierarchical architecture. A single Sb-Ni nanorod is displayed in Figure 1h and i, in agreement with the above SEM observations, where Sb nanoplates with 20 nm in thickness are intercrossed with each other, forming highly porous nanoarchitectures with abundant open areas and electro-active surface sites.

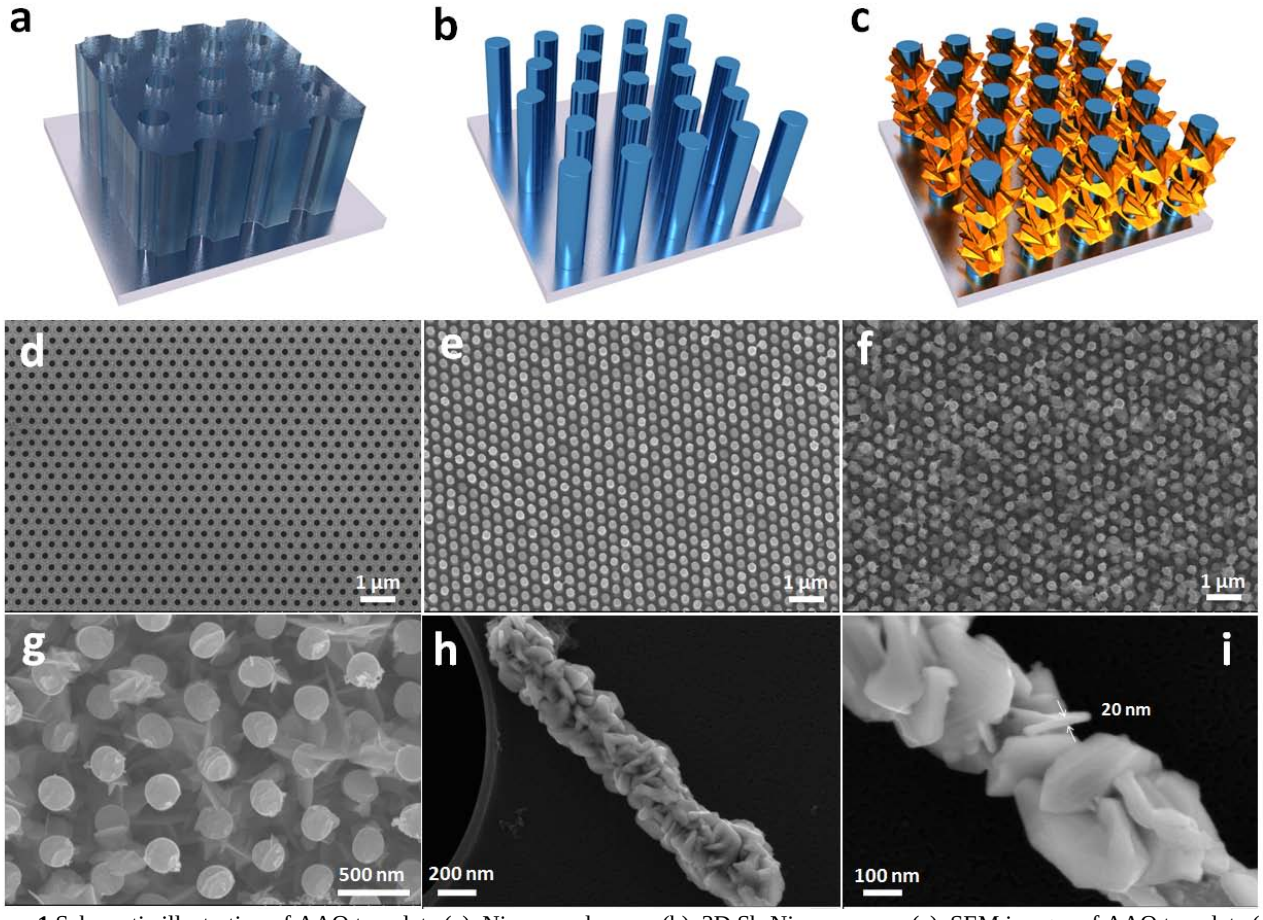

Figure 1 Schematic illustration of AAO template (a), Ni nanorod arrays (b), 3D Sb-Ni nanoarrays (c). SEM images of AAO template (d), Ni nanorod arrays (e), 3D Sb-Ni nanoarrays (f-i).

The crystalline phase of the prepared sample was investigated using X-ray diffraction (XRD), as shown in Figure 2a. Except for the reflections of the substrate (Au) and current collector (Ni), the rest

peaks are in well accordance with the rhombohedral Sb phase (JCPDS No. 35-0732), which confirms the successful fabrication of Sb/Ni heterostructure. Further information of the hierarchical structure was obtained by performing HRTEM characterizations. Figure 2b-d display a dark-field SEM image, line scan profile, and EDX mapping results of a Sb-Ni nanorod, confirming that Sb nanoplates are uniformly distributed on the surface of Ni nanorod. A more close observation on a typical Sb-Ni nanorod is depicted in the HRTEM image (Figure 2e), where irregular Sb nanoplates are firmly anchored on the Ni bone. Figure 2f shows that the Sb crystallites have distinct lattice spacing, in which the lattice fringes with the distances of 0.310 and 0.354 nm correspond to the (012) and (101) planes of rhombohedral Sb, respectively. The fast Fourier transform (FFT) pattern in Figure 2f inset indicates the single crystalline characteristic of Sb.

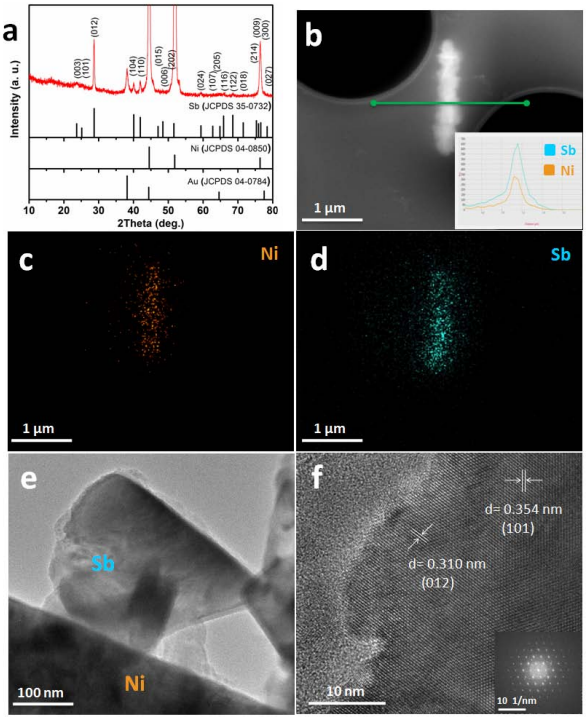

Figure 2 (a) X-ray diffraction pattern of 3D Sb-Ni nanoarrays. (b) Dark-field SEM image of Sb-Ni nanorod, and the corresponding line scan profile (b inset). EDX mapping for (c) Ni and (d) Sb elements. HRTEM images of Sb-Ni nanorod (e), Sb nanoplate (f), and FFT pattern (f inset).

2.2 Na-ion half cell performance

Motivated by the unique structure of 3D Sb-Ni nanoarrays, they are evaluated as binder-free anodes in a Na-ion half cell. Figure 3a shows representative cyclic voltammograms (CVs) of the first three cycles at a scan rate of 0.1 mV s^{-1}. Two strong broad peaks located at 0.42 and 0.37 V are observed in the first sodiation scan, which are ascribed to the formation of a solid electrolyte interface (SEI) layer, and amorphous Na_xSb alloy phase which is subsequently transformed into cubic and hexagonal Na_3Sb through further sodiation [35-37]. In the second sodiation scan, three distinct peaks at 0.67, 0.43 and 0.37 V are clearly observed, corresponding to the multistep sodiation reactions between Sb and Na ions until a hexagonal Na_3Sb alloy is formed [36-38]. The difference between the first and second sodiation scan is mainly ascribed to the formation of SEI layer and the rearrangement of the structure [38-40]. In the desodiation scans, a broad peak ranging from 0.70 to 0.96 V is shown, resulting from the phase transformation from Na_3Sb to Sb [35-37]. Galvanostatic charge-discharge curves of the 3D Sb-Ni nanoarrays anode at a current density of 0.5 A g^{-1} are demonstrated in Figure 3b, which show typical characteristics of Sb anode. The voltage profiles with different flat plateaus suggest the redox reactions associated with Na alloying/dealloying in the discharge and charge curves, which are in good accordance with CVs results in Figure 3a. Furthermore, the voltage profiles of both sodiation and desodiation have excellent reproducibility from 1 to 100 cycles, indicating the stable structure of 3D Sb-Ni nanoarrays and high reversibility during cycling [38].

The cyclic performance of 3D Sb-Ni nanoarrays anodes were investigated at current densities of 0.5 and 1.0 A g^{-1}, respectively. As shown in Figure 3c, the anodes show large reversible capacities and high capacity retentions, which can be associated with the unique hierarchical electrode structure. For example, at a current density of 0.5 A g^{-1}, a reversible capacity of 623 mAh g^{-1} is obtained at the 100th cycle,

which is close to the theoretical capacity of Sb (660 mAh g^{-1}). The capacity retentions after 200 cycles are as high as 80% and 72% at 0.5 and 1.0 A g^{-1}, respectively. These values are much higher than most of reported Sb-based anodes [8, 10, 34, 35, 48]. The capacity fade of 3D Sb-Ni nanoarrays can be ascribed to the increasing thickness of the SEI layer and inevitable volume changes upon cycling. Except for the initial several cycles, the Coulombic Efficiency (CE) is close to 98% at both 0.5 and 1.0 A g^{-1}, suggesting facile ion and electron transport in the 3D Sb-Ni nanoarrays anodes [40-42].

To investigate the effect of 3D heterostructured configuration on the rate capability, 3D Sb-Ni nanoarrays anodes were galvanostatically tested at various current densities from 0.2 to 20 A g^{-1}. As seen in Figure 3d, excellent rate characteristic for 3D Sb-Ni nanoarrays is manifest. It can be reversibly cycled at very high rates of 10 and 20 A g^{-1} and maintains high CEs of about 98%. In the second rate test, 3D Sb-Ni nanoarrays anodes were cycled five times at each current rate. The capacity level is rather stable at each rate, regardless the rate cycling history. More notably, in the second set, it still delivers large capacities of 607 and 580 mAh g^{-1} at 10 and 20 A g^{-1}, respectively, implying the fast transfer of Na ion and electron through 3D Sb-Ni nanoarrays anodes. Further cycling at a low rate of 0.5 A g^{-1} in the third rate test, the capacity retention is around 94% of the capacities at the same rate in the first set, indicating that 3D Sb-Ni nanoarrays have strong structure tolerance to endure greatly varying rates while simultaneously keeping high energy densities. This rate capability and their specific capacities are on the top of reported Sb-based anodes (Figure 3e). Figure 3f presents the corresponding voltage profiles of the anode at various current densities in the first set. In spite of the increasing current densities from 0.2 to 20 A g^{-1}, both charge and discharge voltage profiles have quite similar shapes with minimal increase of the voltage offset. Furthermore, in the second set, when the anode was cycled at 0.5, 1.0, 0.5, and 10 A g^{-1} again, the voltage profiles recovered and are perfectly reproducible in comparison with those of the first set at the same current densities (Figure S1 in the ESM). All these features indicate facile electron transport and small mechanical energy loss in the 3D Sb-Ni nanoarrays anodes.

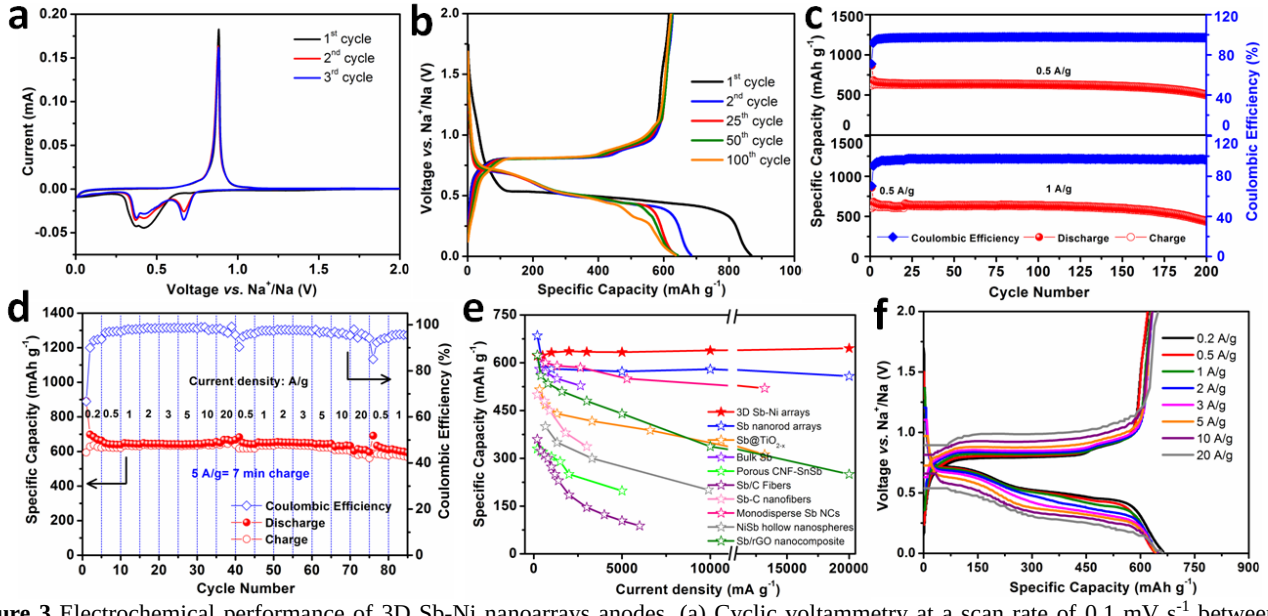

Figure 3 Electrochemical performance of 3D Sb-Ni nanoarrays anodes. (a) Cyclic voltammetry at a scan rate of 0.1 mV s^{-1} between 0.01 to 2.0 V (*vs.* Na^+/Na). (b) Galvanostatic charge/discharge voltage profiles in different cycles at a current density of 0.5 A g^{-1}. (c) Cycling performance at current densities of 0.5 and 1.0 A g^{-1}. (d) Rate performance at various current densities from 0.1 to 20 A g^{-1}. (e) Ragone plots of 3D Sb-Ni nanoarrays anode and other Sb-based SIBs anodes from literature (Sb nanorod arrays: ref. [34], $Sb@TiO_{2-x}$: ref. [20], bulk Sb: ref. [35], porous CNF-SnSb: ref. [38], Sb-C nanofibers: ref. [10], monodisperse Sb NCs: ref. [18], NiSb hollow nanospheres: ref. [21], Sb/rGO nanocomposites: ref. [47], Sb/C fibers: ref. [48]). (f) Charge/discharge voltage profiles at various current densities from 0.1 to 20 A g^{-1}.

2.3 Kinetic and quantitative analysis of Na^+ storage mechanism

To explain the high-rate performance, a detailed electrochemical kinetic of 3D Sb-Ni nanoarrays was analyzed with CV techniques. Figure 4a shows highly similar CVs curves at various scan rates from 0.1 to 10 mV s^{-1}. CV curves could be used to distinguish the diffusion-controlled contribution and capacitive contribution in the reaction based on the slope (*i.e.*, *b* value) calculated by the plots of log (peak current, i_p) to log (scan rate, v) [43]. Usually, b=1 and 0.5 separately indicate that the electrochemical reaction are surface-limited and diffusion-limited with former corresponding to a capacitive behavior and Na^+ ion insetion/extraction. Generally, b values are between 0.5-1, implying both contribute to the reaction. In Figure 4b, 3D Sb-Ni nanoarrays display that b values are 0.82, 0.78 and 0.84 for three cathodic peaks, respectively, indicating the capacitance for the Na-storage reactions in 3D Sb-Ni nanoarrays.

Furthermore, the contribution of the total capacity (Q) storage can be analyzed using Trasatti's method which describes the relationship between the capacity and the sweep rate [44]. The Q involves capacity from surface process (Q_s) and the diffusion-controlled process (Q_d), as given in Equation (1)

$$Q(v) = Q_s + Q_d = Q_s + k(v^{-1/2}) \quad (1)$$

Here k is a constant and v is the potential scan rate. The Q_d is the diffusion-controlled capacity, which is limited by $v^{-1/2}$. The surface capacity (Q_s) will be constant with the scan rate, which can be determined from the plot of capacity (Q) *vs.* $v^{-1/2}$. The extrapolation of the linear fit to the data to the y-intercept ($v^{-1/2}$=0) gives the contribution of capacitive (Q_s), which is calculated to be 131.9 mC cm^{-2} (Figure 4c). Moreover, the relative contributions related to capacitive and diffusion-controlled processes can be identified, as shown in Figure 4d. As the scan rate increases, the role of capacitive contribution further enlarges. The contribution is 84% at a scan rate of 0.1 mV s^{-1}, and reaches 99% at 10 mV s^{-1}. It is reported that capacitive contribution plays a critical role for the structures with high surface area and/or high porosity [14, 45, 46]. Generally, the greater the capacitance is, the better the rate capability is [20, 43]. This fact explains the excellent rate performances of 3D Sb-Ni nanoarrays. To the best of our knowledge, such a stable and robust rate capability has not been reported for Sb-based anodes, which strongly indicates the effectiveness of our electrode design.

2.4 Na-ion full cell performance

To further present the feasibility of the 3D Sb-Ni nanoarrays for Na-storage in practice, a full cell was investigated by consisting 3D Sb-Ni nanoarrays as negative electrodes and P2-$Na_{2/3}Ni_{1/3}Mn_{2/3}O_2$ as positive electrodes. The structure and electrochemical performance characterizations of P2-$Na_{2/3}Ni_{1/3}Mn_{2/3}O_2$ can be found in our previous work [34]. This full cell was tested in a potential window of 1.4-4.0 V. Figure 5a displays CVs of the full cell at a scan rate of 0.5 mV s^{-1}. The cathodic and anodic peaks at 3.4 and 3.7 V correspond to the insertion/extraction into/from P2-$Na_{2/3}Ni_{1/3}Mn_{2/3}O_2$. Another two pairs of peaks at 2.8/3.2 V and 2.77/3.0 V are attributed to the sodiation of Sb and the disodiation of Na_3Sb. The multiple redox reactions are also reflected on the charge/dicharge voltage profile of the full cell (Figure 5a inset), which is in good agremment with the CV results. The excellent reproducibility of CV curves indicates the good stability of electrode materials again. Figure 5b reveals the cycling performance of the full cell, in which it delivers a highly stable capacity over 200 cycles at a current density of 0.5 A g^{-1}. After 200 charge/discharge cycles, it retains a reversible capacity of 579.8 mAh g^{-1} (relative to Sb anode weight), which is 87.8% of the theoretical capacity of Sb (660 mAh g^{-1}). In addition, except the first activation cycles, the cell gives high CEs approaching 98%. The energy density is estimated to be about 100 Wh kg^{-1} (based on the total mass of the positive and negative active materials), which is considered to be an extremely promising value [1].

Furthermore, the full cell also shows a high rate capability, as seen in Figure 5c. It can be cycled at very large rates of 10 and 20 A g^{-1}, and keep stable reversibility, showing the capacities of 526.3 and 434.2 mAh g^{-1}, respectively, in the second set. They correspond to charge time of 3 min 23 s and 1 min 40 s (Figure 5d), respectively, which are sufficient for

high-rate applications [49]. After 75 cycles at various current densities from 0.2 to 20 A g^{-1}, these capacities can still be recovered when the cell went back to the low current density, delivering 539.5 mAh g^{-1} at 0.5 A g^{-1}. Although the current density greatly increases (100 times), the discharge voltage only drops by about 0.16 V, indicating the small polarization and good reaction kinetics in full cell (Figure 5d). The electrochemical performance of the current P2-$Na_{2/3}Ni_{1/3}Mn_{2/3}O_2$//3D Sb-Ni nanoarrays Na-ion full battery is superior to recently reported $Na_3V_2(PO_4)_3$-C//Sb@TiO_2 [20], $Na_{2/3}Ni_{1/3}Mn_{2/3}O_2$//rGO/$Sb_2S_3$ [49], and $Na_{0.4}Mn_{0.54}Co_{0.46}O_2$//NiSb full batteries [21].

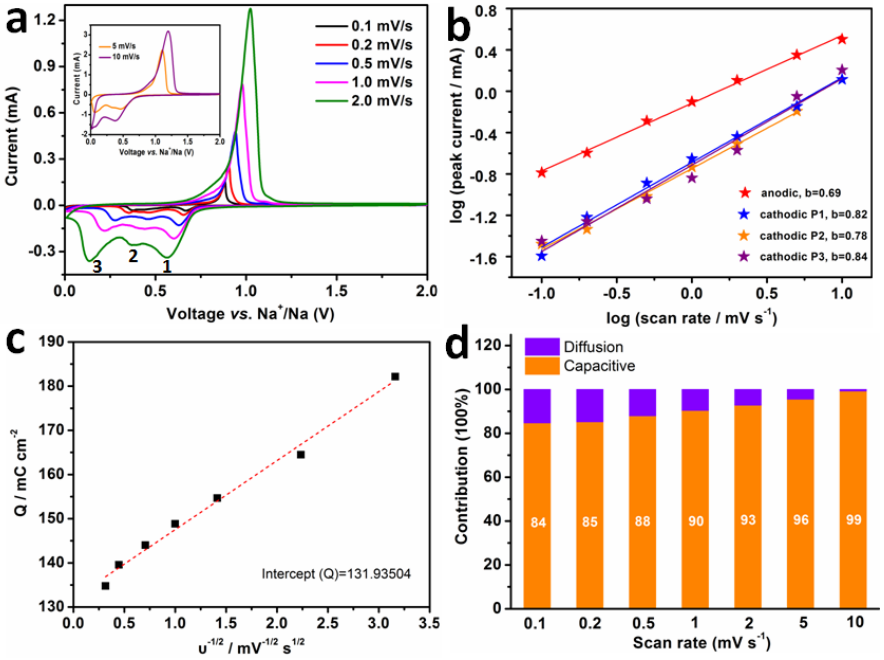

Fiugre 4 Kinetic and quantitative analysis of the Na^+ storage mechanism. (a) CV curves of 3D Sb-Ni nanoarrays at different scan rates from 0.1 to 10 mV s^{-1}. (b) The plots of log (i_p) to log (υ) for cathodic/anodic peaks. (c) Trasatti analysis utilizing the dependence of charge storage on the reciprocal square root of the scan rates. In the plot of capacity (Q) *vs.* $\upsilon^{-1/2}$, the y-intercept corresponds to the infinite sweep rate capacity, $Q_{v=\infty}$. (d) Normalized contribution ratio of capacitive (orange yellow) and diffusion-controlled (blue) capacities at different scan rates calculated using Trasatti analysis described in Equation (1).

2.5 Factors analysis for great electrochemical performance

The excellent electrochemical performance of 3D Sb-Ni nanoarrays can be attributed to the rational design and engineering of the unique nanostructure. Specifically, the high capacity and excellent rate capability are mainly derived from the following structural features. First, Sb nanoplates possess short distance for Na^+ ions diffusion and large electrode-electrolyte contact area for high Na^+ ions flux across the interface. Next, every Ni nanorod provides a direct and fast electron pathway to each Sb nanoplate. Meanwhile, in this open and vertically aligned 3D nanostructure array, highway of electrolyte ions is constructed to realize maximum utilization of electro-active materials at high rates. A possible interfacial sodium storage effect in the Sb/Ni heterogeneous structure may also contribute to the improved electrochemical performance, and the phenomenon has been observed in other reported works [50-54].

Accommodating large volume changes of Sb is another extremely important point to achieve improved rate capability and cycling life. In this work, we designed Sb nanoplates grown on Ni nanorod arrays, where several features are helpful to relieve the volume variations. First, the Ni nanorod serving as a scaffold provides a large surface area for the growth of Sb nanoplates, contributing to well dispersed and immobilized Sb nanoplates, thereby preventing the agglomeration of active materials. Meanwhile, the direct growth of Sb nanoplates on Ni nanorod backbone could provide firm bonding to the

current collector, and Ni skeletons could effectively suppress the adverse mechanical effect from the large volume expansion [55]. The improved capacity and cycle life for the assembly of Sb nanoplates on Ni nanorod arrays present the advantages of our 3D electrode design. As a comparison, Figure S2a and b in the ESM show a planar Sb electrode on Ni foil fabricated by electrodeposition under the same conditions, which is constructed by severely aggregated Sb nanoplates on Ni foil. The planar electrode reveals a dramatic fade in capacity upon cycling and much larger resistances than those of 3D Sb-Ni nanoarrays (Figure S2c-d in the ESM), due to the large volume change and pulverization (Figure S2e-f in the ESM). Second, the presence of sufficient interspace between arrays effectively mitigates the strain caused during Na alloy/dealloy processes. As shown in Figure S3a (in the ESM), the interspace among nanorods was filled with Sb with increasing deposition time, which would reduce the electrolyte accessibility to the space among rods (Figure S4 in the ESM), and volume buffering of Sb could not be achieved during discharge and charge. This results in poor capacity retention ability and rapidly increased resistances (Figure S3b-d in the ESM). Thus, the sufficient interspace is an important parameter for the assembly of Sb nanoplates on Ni nanorods electrode. Third, the void space between these plate-like subunits could buffer the volume change.

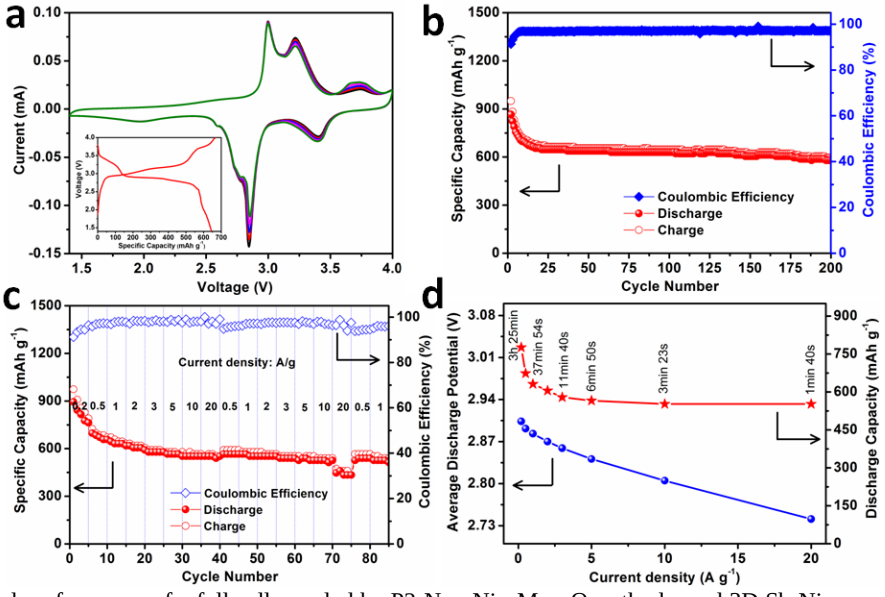

Figure 5 Electrochemical performance of a full cell coupled by P2-$Na_{2/3}Ni_{1/3}Mn_{2/3}O_2$ cathodes and 3D Sb-Ni nanoarrays anodes. (a) CV curves at a scan rate of 0.5 mV s^{-1} and galvanostatic charge/discharge voltage profile (inset) at a current density of 0.5 A g^{-1}. (b) Cycling performance at a current density of 0.5 A g^{-1} (relative to the anode weight) (starting from the 2nd cycle). (c) Rate capability (with respect to the anode weight) at various current densities from 0.1 to 20 A g^{-1}. (d) Respective discharge capacity and average discharge working potential at various current densities.

Last but most important, although the above strategies can alleviate the large volume variation to a certain extent, the volume change still is inevitable, due to inherent nature of Sb. Especially, with further cycling, the mechanical breakdown of Sb is obvious. The advantage of 3D Sb-Ni nanoarrays is manifested when such breakdown happens. A distinct comparison can be found in bare 3D Sb nanorod arrays. In the case of Sb nanorod arrays, because of the loss of electrical contact with the conductive substrate, the whole nanorod beyond the cracking point becomes inaccessible (Figure S5a in the ESM), severely reducing the overall capacity [34]. However, in the case of 3D Sb-Ni nanoarrays, such breakdown has relatively limited influence on the overall capacity since Sb nanoplates that don't fall off can still be connected to the Ni nanorods, as shown in Figure S5b (in the ESM). The overall capacity fades at a comparatively slower pace than that of the nanorods-based nanostructures (Figure S6 in the ESM). The morphology of 3D Sb-Ni nanoarrays after cycling confirmed the above point. Figure 6a and b

display the SEM images of the after-cycled arrays, which are similar to that of before-cycled arrays, implying that this electrode structure can effectively accommodate the huge volume change during sodiation/desodiation. After 200 discharge/charge cycles, due to the repeated huge volume variations, the Sb nanoplates seem to break into smaller nanoplates and have a certain degree of crush in its platy structure, resulting in loose-packed structure (Figure 6c). Despite that, a majority of Sb nanoplates are still tightly attached to Ni nanorods, only showing small capacity decay, confirming the structural stability of 3D Sb-Ni nanoarrays. Figure 6d shows the crystallinity of 3D Sb-Ni nanoarrays after cycling. The distinct lattice spacing is observed, in which the lattice fringe with the distance of 0.221 nm correspond to the (104) planes of rhombohedral Sb.

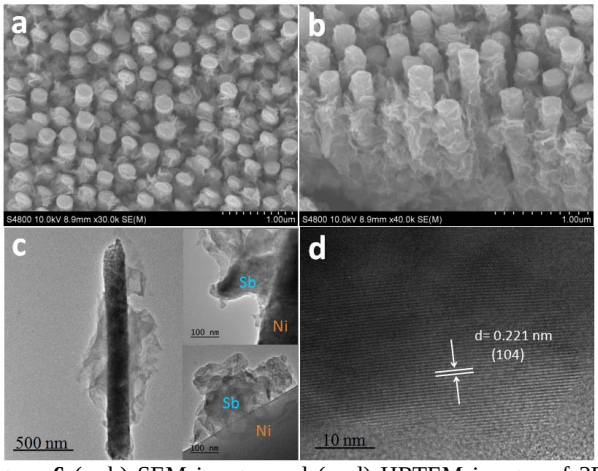

Figure 6 (a, b) SEM images and (c, d) HRTEM images of 3D Sb-Ni nanoarrays anodes after 200 cycles.

3 Conclusions

In summary, we have rationally designed and synthesized hierarchical electrodes constructed by Sb nanoplates on Ni nanorod arrays. This interesting functional heterostructure reveals the synergistic effect of 2D nanoplates, open conductive array structure, and strong structural integrity. The kinetics analysis proves the surface-controlled mechanism in the Na-storage process, clearly indicating that the Na reaction kinetics and durability in 3D Sb-Ni nanoarrays can be elaborately tailored by architecture design. As binder-free SIBs anodes, 3D Sb-Ni nanoarrays show remarkably improved electrochemical performance for both Na-ion half cells and full cells. It is expected that this design strategy is applicable to modulating other electrodes for advanced energy storage systems.

4 Experimental

4.1 Material synthesis

The through-pore AAO templates with conductive substrate were fabricated by an anodization process followed by ion coating. The detailed process can be found in our previous work [34]. Ni nanorod arrays were electrodeposited inside AAO templates at a constant current density of 2.0 mA cm^{-2} in an electrolytic bath containing $NiCl_2$, $NiSO_4$, and H_3BO_3. The electrodeposition was conducted in a two-electrode cell with AAO template as the working electrode and Ni foil as counter electrode. Ni nanorod arrays are released by dissolving the AAO template in a NaOH solution (3.0 M) for 30 min, followed by a rinsing process with deionized water. The Ni nanorod arrays were immersed in an electrolytic bath containing $SbCl_3$ and $Na_3C_6H_5O_7{\cdot}2H_2O$, and then placed in the vacuum oven for a while. 3D Sb-Ni nanoarrays were prepared by electrodepositing Sb on Ni nanorod arrays at a constant current density of 1.0 mA cm^{-2}. The electrodeposition was also conducted in a two-electrode cell with Ni nanorod arrays as the working electrode and Pt foil as counter electrode.

4.2 Sample characterization

SEM measurements were performed on a Hitachi S4800 instrument with voltages of 10 kV. HRTEM measurement was taken on a FEI Titan 80-300 operated at 300 KV. XRD measurement was carried out on a Bruker-axs Discover D8 applying Cu Kα (1.54056 Å) radiation equipment. For post-cycling SEM measurement, 3D Ni-Sb arrays electrodes after electrochemical cycling tests were carefully disassembled and washed with PC solution in glove box, and dried at 60°C in a vacuum oven.

4.3 Electrochemical measurements

Electrochemical measurements of half cells were conducted using CR2032 coin-type cells with Na

metal as both counter and reference electrode. 3D Sb-Ni nanoarrays were employed as anodes without any additives of conductive carbon and binder. The coin batteries were assembled in a nitrogen-filled glove box with a glass fiber separator (Whatman, GFB/55) and the electrolyte solution of 1.0 M $NaClO_4$ in EC: PC (1:1 by volume) with the addition of 5% fluoroethylene carbonate (FEC). The galvanostatic charge-discharge tests were performed at various current densities on LAND-CT2001A test system (Wuhan, China). Cyclic voltammogram (CV) was tested on a BioLogic VSP potentiostat. Electrochemical impedance spectroscopy (EIS) was also taken on a BioLogic VSP potentiostat with frequency of 1 MHz to 10 mHz at the charge state (2.0 V). All of these experiments were conducted at room temperature.

Electrochemical measurements of full cells were taken using CR2032 coin-type cells with 3D Ni-Sb nanoarrays as negative electrodes and P2-$Na_{2/3}Ni_{1/3}Mn_{2/3}O_2$ as positive electrodes. P2-$Na_{2/3}Ni_{1/3}Mn_{2/3}O_2$ was prepared by mixing 80% P2-$Na_{2/3}Ni_{1/3}Mn_{2/3}O_2$, 10% acetylene black, and 10% poly(vinylidene fluoride) (PVDF) by weight with an appropriate amount of 1-methyl-2-pyrrolidinone (NMP). The above mixture was pressed onto an aluminum foil which served as a current collector. The cathode was dried at 120 °C in vacuum for 12 h. The full cell was assembled using an electrolyte solution of 1.0 M $NaClO_4$ in EC: PC (1:1 by volume) with 5% FEC and galvanostatically cycled with the voltage range of 4.0 to 1.4 V. To ensure a suitable positive-to-negative (P/N) capacity ratio for proper cell balance, the P2-$Na_{2/3}Ni_{1/3}Mn_{2/3}O_2$ to Sb nanorod arrays mass loading ratio was about 20.

Acknowledgements

This work is financially supported by the European Research Council (ThreeDsurface, 240144), European Research Council (HiNaPc, 737616), Bundesministerium für Bildung und Forschung (ZIK-3DNanoDevice, 03Z1MN11), and German Research Foundation (DFG: LE 2249_4-1).

Electronic Supplementary Material: Supplementary material (voltage profiles at various current densities in different sets, SEM images and electrochemical performance of planar Sb electrode on Ni foil and 3D Sb-Ni nanoarrays with insufficient interspace, Schematic illustration of transport mechanism of Na ions in various Sb structures, comparison of cycling performance between bare Sb nanorod arrays and 3D Sb-Ni nanoarrays) is available in the online version of this article at http://dx.doi.org/10.1007/s12274-***-****-*

References

[1] Hasa, I.; Passerini, S.; Hassoun, J. A rechargeable sodium-ion battery using a nanostructured Sb–C anode and P2-type layered $Na_{0.6}Ni_{0.22}Fe_{0.11}Mn_{0.66}O_2$ cathode. *RSC Adv.* **2015**, *5*, 48928-48934.

[2] Palomares, V.; Serras, P.; Villaluenga, I.; Hueso, K. B.; Carretero-Gonzalez, J.; Rojo, T. Na-ion batteries, recent advances and present challenges to become low cost energy storage systems. *Energy Environ. Sci.* **2012**, *5*, 5884-5901.

[3] Kim, S. W.; Seo, D. H.; Ma, X.; Ceder, G.; Kang, K. Electrode materials for rechargeable sodium-ion batteries: potential alternatives to current lithium-ion batteries. *Adv. Energy Mater.* **2012**, *2*, 710-721.

[4] Hong, S. Y.; Kim, Y.; Park, Y.; Choi, A.; Choi, N.-S.; T. Lee, K. Charge carriers in rechargeable batteries: Na ions *vs.* Li ions. *Energy Environ. Sci.* **2013**, *6*, 2067-2081.

[5] Slater, M. D.; Kim, D.; Lee, E.; Johnson, C. S. Sodium-ion batteries. *Adv. Funct. Mater.* **2013**, *23*, 947-958.

[6] Stevens, D. A.; Dahn, J. R. High capacity anode materials for rechargeable sodium-ion batteries. *J. Electrochem. Soc.* **2000**, *147*, 1271-1273.

[7] Jeong, G.; Kim, Y.-U.; Kim, H.; Kim,Y.-J.; Sohn, H.-J. Prospective materials and applications for Li secondary batteries. *Energy Environ. Sci.* **2011**, *4*, 1986-2002.

[8] Hu, L.; Zhu, X.; Du, Y.; Li, Y.; Zhou, X.; Bao, J. A chemically coupled antimony/multilayer graphene hybrid as a high-performance anode for sodium-ion batteries. *Chem. Mater.* **2015**, *27*, 8138-8145.

[9] Xu, Y.; Liu, Q.; Zhu, Y.; Liu, Y.; Langrock, A.; Zachariah, M. R.; Wang, C. Uniform nano-Sn/C composite anodes for lithium ion batteries. *Nano Lett.* **2013**, *13*, 470-474.

[10] Xiao, L.; Cao, Y.; Xiao, J.; Wang, W.; Kovarik, L.; Nie, Z.; Liu, J. High capacity, reversible alloying reactions in SnSb/C nanocomposites for Na-ion battery applications. *Chem. Commun.* **2012**, *48*, 3321-3323.

[11] Chevrier, V. L.; Ceder, G. Challenges for Na-ion negative electrodes. *J. Electrochem. Soc.* **2011**, *158*, A1011-A1014.

[12] Wu, L.; Lu, H.; Xiao, L.; Ai, X.; Yang, H.; Cao, Y. Electrochemical properties and morphological evolution of pitaya-like Sb@C microspheres as high-performance anode for sodium ion batteries. *J. Mater. Chem. A*, **2015**, *3*, 5708-5713.

[13] Xie, X.; Kretschmer, K.; Zhang, J.; Sun, B.; Su, D.; Wang, G. Sn@CNT nanopillars grown perpendicularly on carbon paper: a novel free-standing anode for sodium ion batteries. *Nano Energy* **2015**, *13*, 208-217.

[14] Chao, D.; Zhu, C.; Yang, P.; Xia, X.; Liu, J.; Wang, J.; Fan, X.; Savilov, S. V.; Lin, J.; Fan, H. J.; Shen, Z. X. Array of nanosheets render ultrafast and high-capacity Na-ion storage by tunable pseudocapacitance. *Nature Commun*. **2016**, *7*, 12122-12129.

[15] Lee, G.-H.; Shim, H.-W.; Kim, D.-W. Superior long-life and high-rate Ge nanoarrays anchored on Cu/C nanowire frameworks for Li-ion battery electrodes. *Nano Energy* **2015**, *13*, 218-225.

[16] Song, X.; Li, X.; Bai, Z.; Yan, B.; Li, D.; Sun, X. Morphology-dependent performance of nanostructured Ni_3S_2/Ni anode electrodes for high performance sodium ion batteries. *Nano Energy* **2016**, *26*, 533-540.

[17] Ko, Y. N.; Kang, Y. C. Electrochemical properties of ultrafine Sb nanocrystals embedded in carbon microspheres for use as Na-ion battery anode materials. *Chem. Commun.* **2014**, *50*, 12322-12324.

[18] He, M.; Kravchyk, K.; Walter, M.; Kovalenko, M. V. Monodisperse antimony nanocrystals for high-rate Li-ion and Na-ion battery anodes: nano versus bulk. *Nano Lett.* **2014**, *14*, 1255-1262.

[19] Hou, H.; Jing, M.; Yang, Y.; Zhu, Y.; Fang, L.; Song, W.; Pan, C.; Yang, X.; Ji, X. Sodium/lithium storage behavior of antimony hollow nanospheres for rechargeable batteries. *ACS Appl. Mater. Interfaces* **2014**, *6*, 16189-16196.

[20] Wang, N.; Bai, Z.; Qian, Y.; Yang, J. Double-walled Sb@TiO_{2-x} nanotubes as a superior high-rate and ultralong-lifespan anode material for Na-ion and Li-ion batteries. *Adv. Mater.* **2016**, *1*, 4126-4133.

[21] Liu, J.; Yang, Z.; Wang, J.; Gu, L.; Maier, J.; Yu, Y. Three-dimensionally interconnected nickel–antimony intermetallic hollow nanospheres as anode material for high-rate sodium-ion batteries. *Nano Energy* **2015**, *16*, 389-398.

[22] Zhang, N.; Liu, Y.; Lu, Y.; Han, X.; Cheng, F.; Chen, J. Spherical nano-Sb@C composite as a high-rate and ultra-stable anode material for sodium-ion batteries. *Nano Research* **2015**, *8*, 3384-3393.

[23] Liu, S.; Feng, J.; Bian, X.; Liu, J.; Xu, H. The morphology-controlled synthesis of a nanoporous-antimony anode for high-performance sodium-ion batteries. *Energy Environ. Sci.* **2016**, *9*, 1229-1236.

[24] Wang, J.; Du, N.; Zhang, H.; Yu, J.; Yang, D. Cu–Ge core–shell nanowire arrays as three-dimensional electrodes for high-rate capability lithium-ion batteries. *J. Mater. Chem.* **2012**, *22*, 1511-1515.

[25] Lee, C. W.; Kim, J.-C.; Park, S.; Song, H. J.; Kim, D.-W. Highly stable sodium storage in 3-D gradational Sb–NiSb–Ni heterostructures. *Nano Energy* **2015**, *15*, 479-489.

[26] Xu, Y.; Zhou, M.; Wen, L.; Wang, C.; Zhao, H.; Mi, Y.; Liang, L.; Fu, Q.; Wu, M.; Lei, Y. Highly ordered three-dimensional Ni-TiO_2 nanoarrays as sodium ion battery anodes. *Chem. Mater.* **2015**, *27*, 4274-4280.

[27] Ke, F.-S.; Huang, L.; Solomon, B. C.; Wei, G-Z.; Xue, L.-J.; Zhang, B.; Li, J.-T.; Zhou, X.-D.; Sun, S.-G. Three-dimensional nanoarchitecture of Sn–Sb–Co alloy as an anode of lithium-ion batteries with excellent lithium storage performance. *J. Mater. Chem.* **2012**, *22*, 17511-17517.

[28] Wang, J.; Du, N.; Zhang, H.; Yu, J.; Yang, D. Cu–Sn core–shell nanowire arrays as three-dimensional electrodes for lithium-ion batteries. *J. Phys. Chem. C* **2011**, *115*, 23620-23624.

[29] Ryou, M. H.; Kim, J.; Lee, I.; Kim, S.; Jeong, Y. K.; Hong, S.; Ryu, J. H.; Kim, T. S.; Park, J. K.; Lee, H.; Choi, J. W. Mussel-inspired adhesive binders for high-performance silicon nanoparticle anodes in lithium-ion batteries. *Adv. Mater.* **2013**, *25*, 1571-1576.

[30] Zhao, F.; Han, N.; Huang, W.; Li, J.; Ye, H.; Chen, F.; Li, Y. Nanostructured CuP_2/C composites as high-performance anode materials for sodium ion batteries. *J. Mater. Chem. A* **2015**, *3*, 21754-21759.

[31] Ellis, B. L.; Knauth, P.; Djenizian, T. Three-Dimensional Self-Supported Metal Oxides for Advanced Energy Storage. *Adv. Mater.* **2014**, *26*, 3368-3397.

[32] Fan, M.; Chen, Y.; Xie, Y.; Yang, T.; Shen, X.; Xu, N.; Yu, H.; Yan, C. Half-cell and full-cell applications of highly stable and binder-rree sodium ion batteries based on Cu_3P nanowire anodes. *Adv. Funct. Mater.* **2016**, *26*, 5019-5027.

[33] Liu, Y.; Xu, Y.; Zhu, Y.; Culver, J. N.; Lundgren, C. A.; Xu, K.; Wang, C. Tin-coated viral nanoforests as sodium-ion battery anodes. *ACS Nano* **2013**, *7*, 3627-3634.

[34] Liang, L.; Xu, Y.; Wang, C.; Wen, L.; Fang, Y.; Mi, Y.; Zhou, M.; Zhao, H.; Lei, Y. Large-scale highly ordered Sb nanorod array anodes with high capacity and rate capability for sodium-ion batteries. *Energy Environ. Sci.* **2015**, *8*, 2954-2962.

[35] Darwiche, A.; Marino, C.; Sougrati, M. T.; Fraisse, B.; Stievano, L.; Monconduit, L. Better cycling performances of bulk Sb in Na-ion batteries compared to Li-Ion systems: an unexpected electrochemical mechanism. *J. Am. Chem. Soc*. **2012**, *134*, 20805-20811.

[36] Baggetto, L.; Ganesh, P.; Sun, C.-N.; Meisner, R. A.; Zawodzinski, T. A.; Veith, G. M. Intrinsic thermodynamic and kinetic properties of Sb electrodes for Li-ion and Na-ion batteries: experiment and theory. *J. Mater. Chem. A* **2013**, *1*, 7985-7994.

[37] Baggetto, L.; Hah, H.-Y.; Jumas, J.-C.; Johnson, C. E.; Johnson, J. A.; Keum, J. K.; Bridges, C. A.; Veith, G. M. Influence of pore structure on electric double-layer capacitance of template mesoporous carbons. *J. Power Sources* **2014**, *267*, 329-336.

[38] Ji, L.; Gu, M.; Shao, Y.; Li, X.; Engelhard, M. H.; Arey, B. W.; Wang, W.; Nie, Z.; Xiao, J.; Wang, C.; Zhang, J. G.; Liu, J. Controlling SEI formation on SnSb-porous carbon nanofibers for improved Na ion storage. *Adv. Mater.* **2014**, *26*, 2901-2908.

[39] Zhou, X.; Zhong, Y.; Yang, M.; Hu, M.; Wei, J.; Zhou, Z. Sb nanoparticles decorated N-rich carbon nanosheets as anode materials for sodium ion batteries with superior rate capability and long cycling stability. *Chem. Commun.* **2014**, *50*, 12888-12891.

[40] Luo, B.; Wang, B.; Li, X. L.; Jia, Y. Y.; Liang, M. H.; Zhi, L. J. Graphene-confined Sn nanosheets with enhanced lithium storage capability. *Adv. Mater.* **2012**, *24*, 3538-3543.

[41] He, C.; Wu, S.; Zhao, N.; Shi, C.; Liu, E.; Li, J. Carbon-encapsulated Fe_3O_4 nanoparticles as a high-rate lithium ion battery anode material. *ACS Nano* **2013**, *7*, 4459-4469.

[42] Jia, X. L.; Chen, Z.; Cui, X.; Peng, Y. T.; Wang, X. L.;

Wang, G.; Wei, F.; Lu, Y. F. Building robust architectures of carbon and metal oxide nanocrystals toward high-performance anodes for lithium-ion batteries. *ACS Nano* **2012**, *6*, 9911-9919.

[43] Zhang, K.; Hu, Z.; Liu, X.; Tao, Z. L.; Chen, J. $FeSe_2$ microspheres as a high-performance anode material for Na-ion batteries. *Adv. Mater.* **2015**, *27*, 3305-3309.

[44] Ardizzone, S.; Fregonara, G.; Trasatti, S. "Inner" and "outer" active surface of RuO_2 electrodes. *Electrochim. Acta* **1989**, *35*, 263–267.

[45] Brezesinski, T.; Wang, J.; Tolbert, S. H.; Dunn, B. Ordered mesoporous α-MoO_3 with iso-oriented nanocrystalline walls for thin-film pseudocapacitors. *Nat. Mater.* **2010**, *9*, 146-151.

[46] Chen, Z.; Augustyn, V.; Jia, X.; Xiao, Q.; Dunn, B.; Lu, Y. High-Performance sodium-ion pseudocapacitors based on hierarchically porous nanowire composites. *ACS Nano*, **2012**, *6*, 4319-4327.

[47] Zhang, W.; Liu, Y.; Chen, C.; Li, Z.; Huang, Y.; Hu, X. Flexible and binder-free electrodes of Sb/rGO and $Na_3V_2(PO_4)_3$/rGO nanocomposites for sodium-ion batteries. *Small* **2015**, *11*, 3822-3829.

[48] Zhu, Y.; Han, X.; Xu, Y.; Liu, Y.; Zheng, S.; Xu, K.; Hu, L.; Wang, C. Electrospun Sb/C fibers for a stable and fast sodium-ion battery anode. *ACS Nano* **2013**, *7*, 6378-6386.

[49] Yu, D. Y. W.; Prikhodchenko, P. V.; Mason, C. W.; Batabyal, S. K.; Gun, J.; Sladkevich, S.; Medvedev, A. G.; Lev, O. High-capacity antimony sulphide nanoparticledecorated graphene composite as anode for sodium-ion batteries. *Nat. Commun.* **2013**, *4*, 2922-2928.

[50] Yang, Y.; Fan, X.; Casillas, G.; Peng, Z.; Ruan, G.; Wang, G.; Yacaman, M. J.; Tour, J. M. Three-dimensional nanoporous Fe_2O_3/Fe_3C-graphene heterogeneous thin films for lithium-Ion batteries. *ACS Nano* **2014**, *8*, 3939-3946.

[51] Zhukoskii, Y. F.; Balaya, P.; Kotomin, E. A.; Maier, J. Evidence for interfacial-storage anomaly in nanocomposites for lithium batteries from first-principles simulations. Phys. *Rev. Lett.* **2006**, *96*, 058302.

[52] Jamnik, J.; Maier, J. Nanocrystallinity effects in lithium battery materials Aspects of nano-ionics. Part IV. *Phys. Chem. Chem. Phys.* **2003**, *5*, 5215-5220.

[53] Shin, J.-Y.; Samuelis, D.; Maier, J. Sustained lithium-storage performance of hierarchical, nanoporous anatase TiO_2 at high rates: emphasis on interfacial storage phenomena. *Adv. Funct. Mater.* **2011**, *21*, 3464-3472.

[54] Balaya, P. Size effects and nanostructured materials for energy applications. *Energy Environ. Sci.* **2008**, *1*, 645-654.

[55] Nam, D.-H.; Hong, K.-S.; Lim, S.-J.; Kim, M.-J.; Kwon, H.-S. High-performance Sb/Sb_2O_3 anode materials using a polypyrrole nanowire network for na-ion batteries. *Small* **2015**, *11*, 2885-2892.

Electronic Supplementary Material

Hierarchical Sb-Ni nanoarrays as robust binder-free anodes for high-performance sodium-ion half cells and full Cells

Liying Liang, Yang Xu, Liaoyong Wen, Yueliang Li, Min Zhou, Chengliang Wang, Huaping Zhao, Ute Kaiser, and Yong Lei (✉)

[1] *Institute of Physics & IMN MacroNano (ZIK), Ilmenau University of Technology, Professor Schmidt Strasse 26, 98693 Ilmenau, Germany*
[2] *Central Facility for Electron Microscopy, Electron Microscopy Group of Materials Science, Ulm University, Albert-Einstein-Allee 11, 89081 Ulm, Germany*

Supporting information to DOI 10.1007/s12274-****-****-*

Address correspondence to yong.lei@tu-ilmenau.de

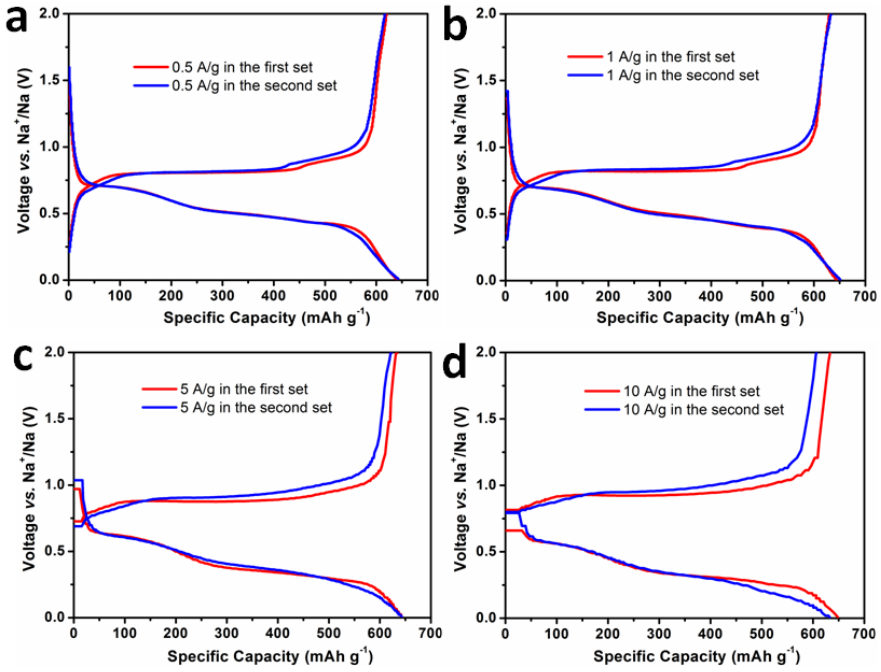

Figure S1 Galvanostatic charge/discharge voltage profiles at various current densities in different sets.

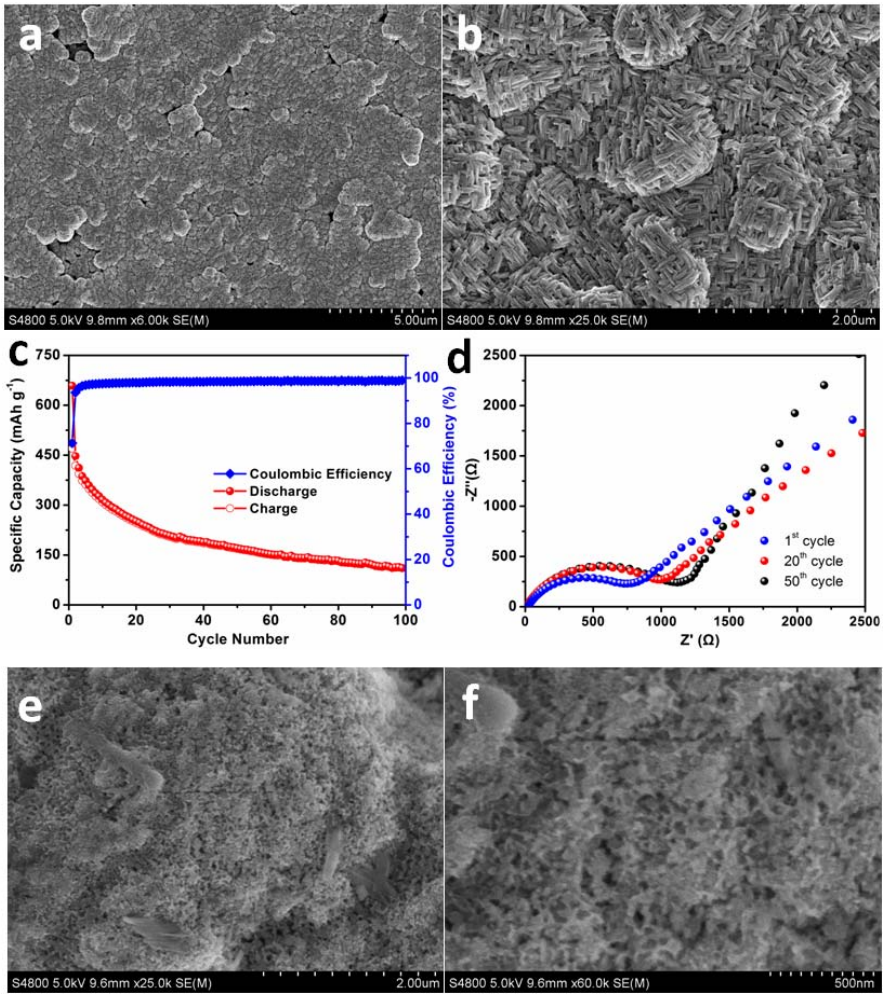

Figure S2 (a and b) SEM images of planar Sb electrode on Ni foil. (c) Cycling performance of planar Sb electrode on Ni foil at a current density of 0.5 A g^{-1}. (d) Nyquist plots of planar Sb electrode at charge state (2.0 V) from 1 MHz to 10 mHz. (e and f) SEM iamges of cycled planar Sb electrode after 200 cycles at 0.5 A g^{-1}.

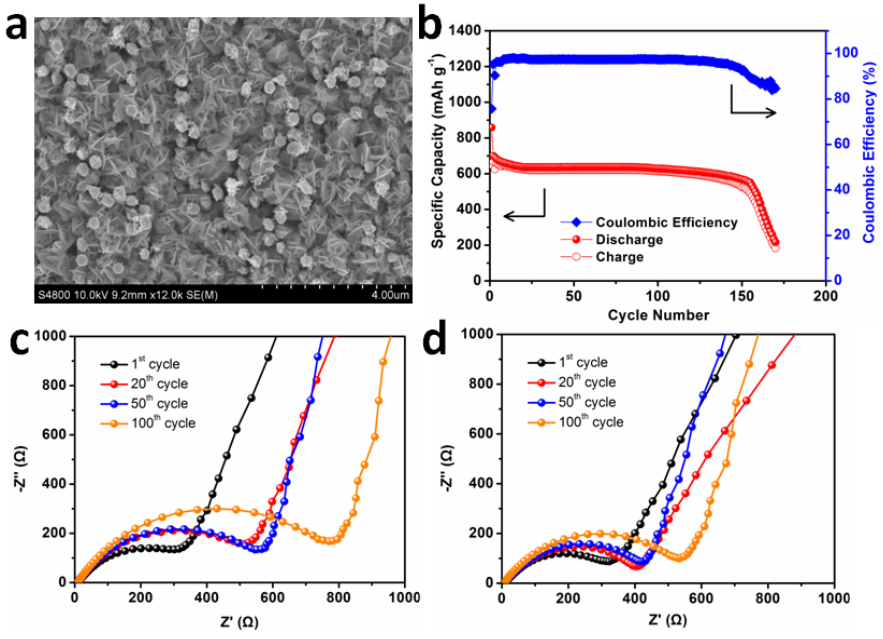

Figure S3 3D Sb-Ni nanoarrays with insufficient interspace: (a) SEM image, (b) Cycling performance at 0.5 A g^{-1}, (c) Nyquist plots at charge state (2.0 V) from 1 MHz to 10 mHz. (d) Nyquist plots of 3D Sb-Ni nanoarrays at charge state (2.0 V) from 1 MHz to 10 mHz.

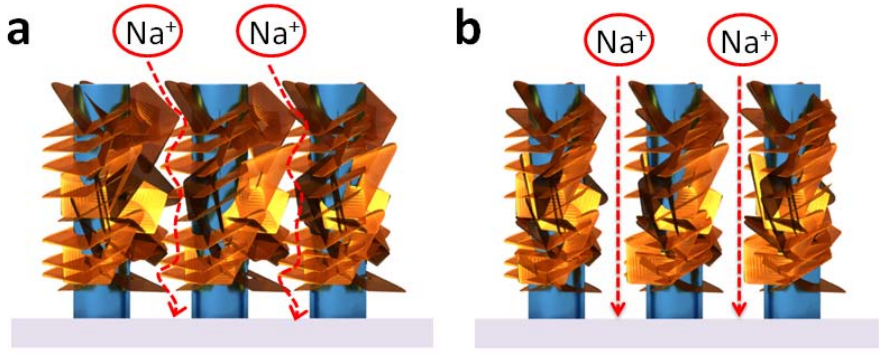

Figure S4 Schematic illustration of transport mechanism of Na ions in 3D Sb-Ni nanoarrays without (a) and with (b) sufficient interspace.

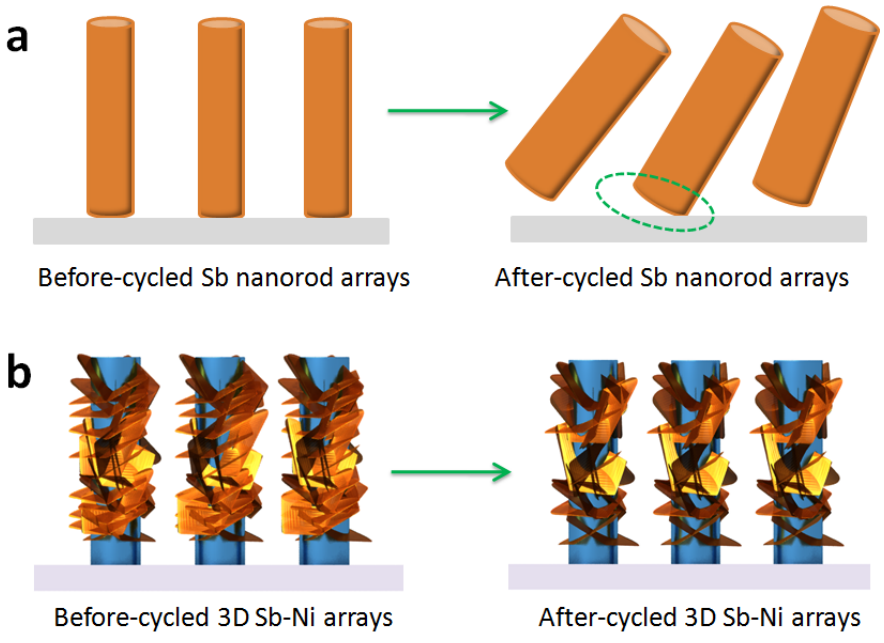

Figure S5 Schematic illustration of after-cycled fade mechanism of bare Sb nanorod arrays (a) and 3D Sb-Ni nanoarrays (b).

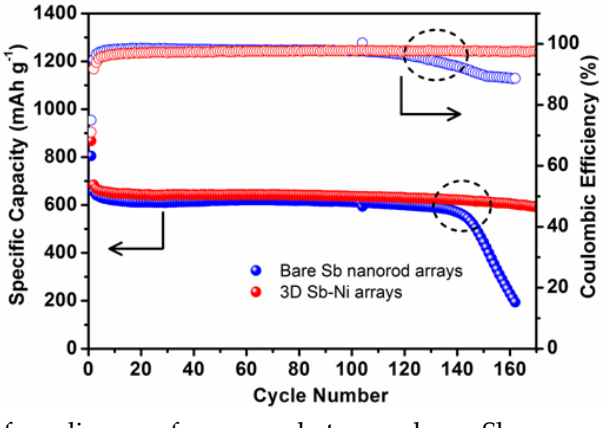

Figure S6 The comparison of cycling performance between bare Sb nanorod arrays and 3D Sb-Ni nanoarrays.